

Optical Measurements of Three-Dimensional Microscopic Temperature Distributions Around Gold Nanorods Excited by Localized Surface Plasmon Resonance

JunTaek Oh,^{1,§} Gu-Haeng Lee,² Jinsung Rho,^{3,§} Seungwoo Shin,^{1,4} Bong Jae Lee,^{3,*} Yoonkey Nam,^{2,†} and YongKeun Park^{1,4,5,‡}


¹*Department of Physics, Korea Advanced Institute of Science and Technology (KAIST), Daejeon 34141, Republic of Korea*

²*Department of Bio and Brain Engineering, KAIST, Daejeon 34141, Republic of Korea*

³*Department of Mechanical Engineering, KAIST, Daejeon 34141, Republic of Korea*

⁴*KAIST Institute for Health Science and Technology, KAIST, Daejeon 34141, Republic of Korea*

⁵*TomoCube Inc., Daejeon 34051, Republic of Korea*

 (Received 7 November 2018; revised manuscript received 23 January 2019; published 24 April 2019)

The measurement and control of the temperature in microscopic systems, which are increasingly required in diverse applications, are fundamentally important. Yet, the measurement of the three-dimensional (3D) temperature distribution in microscopic systems has not been demonstrated. We propose and experimentally demonstrate the measurement of the 3D temperature distribution by exploiting the temperature dependency of the refractive index (RI). Measurement of the RI distribution of water makes it possible to quantitatively obtain its 3D temperature distribution above a glass substrate coated with gold nanorods with submicrometer resolution in a temperature range of 100 °C and with a sensitivity of 2.88 °C. The 3D temperature distributions that are obtained enable various thermodynamic properties including the maximum temperature, heat flux, and thermal conductivity to be extracted and analyzed quantitatively.

DOI: [10.1103/PhysRevApplied.11.044079](https://doi.org/10.1103/PhysRevApplied.11.044079)

I. INTRODUCTION

Three-dimensional (3D) temperature distribution, one of the essential physical quantities for indicating the state of a system, provides invaluable insights of diverse thermal-induced applications in micrometer-sized systems, including photothermal therapy [1], modulation of neural activity [2,3], drug delivery [4], and microfluidics [5]. Previously, to identify the temperature change of the systems, a number of approaches have been developed, such as infrared thermometry [6–8], fluorescent microscopy [9–12], and quantitative phase microscopy and interferometric microscopy [13–16]. However, previous tools only measured the two-dimensional (2D) temperature distribution [6] with labeling agencies [9–12] or employed the heat diffusion equation to retrieve both 2D and 3D temperature distributions [13,14].

To overcome these limitations, we propose a straightforward approach to measure the 3D temperature distribution

by exploiting the temperature dependency of water refractive index (RI) [17]. Optical diffraction tomography (ODT) is employed to reconstruct the 3D RI distribution of heated water with multiple illuminations at various incident angles [18–20]. Using *a priori* information about the temperature dependency of the water RI, the 3D temperature distribution of water above a glass substrate coated with gold nanorods (GNRs) is reconstructed from the measured 3D RI distribution. We experimentally demonstrate the feasibility of the proposed method with statistical analysis and numerical simulation, which solves the steady-state heat diffusion equation. We verify that the measured 3D temperature distributions provide diverse thermodynamic properties of the system, including the maximum temperature, heat flux, and thermal conductivity.

II. PRINCIPLE

The main concept of 3D temperature measurement is depicted in Fig. 1. The measurement exploits the temperature dependency of the RI of water. In practice, this involves obtaining the 3D temperature distribution of hot water from the 3D distribution of the RI, which is reconstructed using the principle of ODT [18,19].

*Bongjae.lee@kaist.ac.kr

†ynam@kaist.ac.kr

‡yk.park@kaist.ac.kr

§Current address: Samsung Electronics-Mechatronics R&D Center, Hwaseong, 18448, Republic of Korea

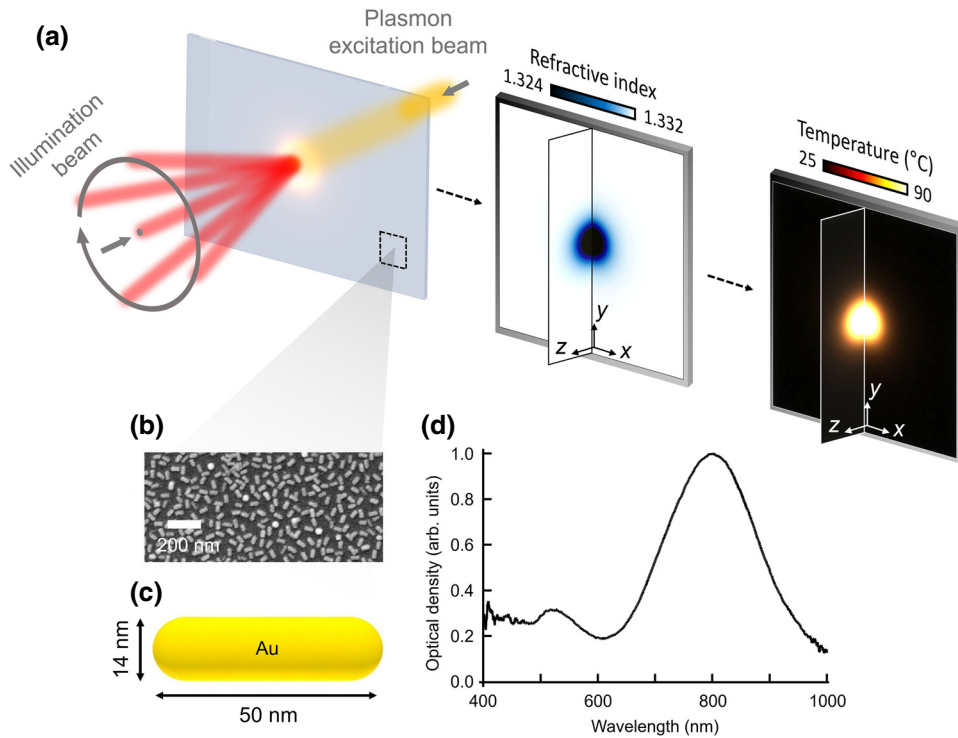


FIG. 1. (a) A plasmon excitation beam (the yellow line) is focused on the bottom cover glass coated with GNRs to raise the temperature of the water. The holograms measured at various illumination angles (red lines) are used to reconstruct the 3D RI distribution of the heat, from which the 3D temperature distribution is to be obtained. (b) SEM image of measured GNRs coated sample. (c) Specification of GNRs. 307 GNRs are statistically analyzed. The mean diameter, length, and aspect ratio are 14.4 nm, 50.1 nm, and 3.60, respectively. (d) The absorption spectrum of GNRs-coated cover glass.

The temperature dependency of the RI of water can be expressed using an empirical equation

$$\Delta T = \sum_i \beta_i \Delta n^i, \quad (1)$$

where ΔT is the temperature change, Δn is the RI change of water, and β_i are empirical coefficients [17] (see Appendix A). The proposed concept is experimentally demonstrated by using GNRs and by generating heat in the water using localized surface plasmon resonance [21]. The GNRs are synthesized for the maximum absorption efficiency at the wavelength of the excitation source. Distilled water is loaded between two cover glasses, and the bottom cover glass is coated with GNRs to control the temperature distribution of water [22,23] [Figs. 1(b)–1(d)].

III. METHODS

A. Experimental set up

ODT, which is employed to measure the RI distribution of water in three dimensions [18,19,24,25], reconstructs the 3D RI distribution by measuring multiple 2D holograms at various illumination angles [19]. These holograms are acquired by using a Mach-Zehnder interferometer equipped with a digital micromirror device (DMD) [26]. A continuous wave (cw) infrared (IR) laser diode is utilized to excite the GNRs on the bottom glass cover and raise the temperature of the fluidic system [Fig. 2(a)].

The optical fields diffracted by heated water at various illumination angles are retrieved from the obtained

multiple holograms based on the Fourier transform method [27] [Fig. 2(b)]. The 3D RI distribution of hot water is constructed by mapping the retrieved optical fields onto 3D Fourier space based on the principle of ODT [18,28] [Fig. 2(c)]. Because of the limited numerical aperture (NA) of the objective lens, side scattering signal cannot be collected [29]. In order to compensate for this limitation, we use an iterative regularization method with two physical constraints: (i) the reconstructed RI value of water cannot be higher than that of water at room temperature and (ii) the RI of the glass substrate remains constant because the changes in the RI of glass within the changed temperature range are negligible [17,30] (see Appendix A). Using these two constraints, the missing information in the Fourier space is filled [Fig. 2(c)]. Because the region of initially mapped data in the Fourier space is modified as well, the initial data is recovered and an approximate solution is obtained [31]. We repeat this iterative regularization process to obtain a converged 3D RI tomogram as illustrated in Fig. 2(d). As the last step, we reconstruct the 3D temperature distribution using Eq. (1) [Fig. 2(e)].

The 3D RI distribution of a sample is reconstructed by employing the principle of optical diffraction tomography (ODT) [18,19]. A commercial ODT set up (HT-1H, Tomocube Inc., Republic of Korea) is customized for the experiment. A HeNe laser (HNL150R, $\lambda = 633$ nm, 15 mW, Thorlabs Inc., USA) is used as a light source. The beam is split into two branches, the reference and sample arms, respectively. A DMD (DLP LightCrafter 6500, Texas Instruments Inc., USA) is exploited to

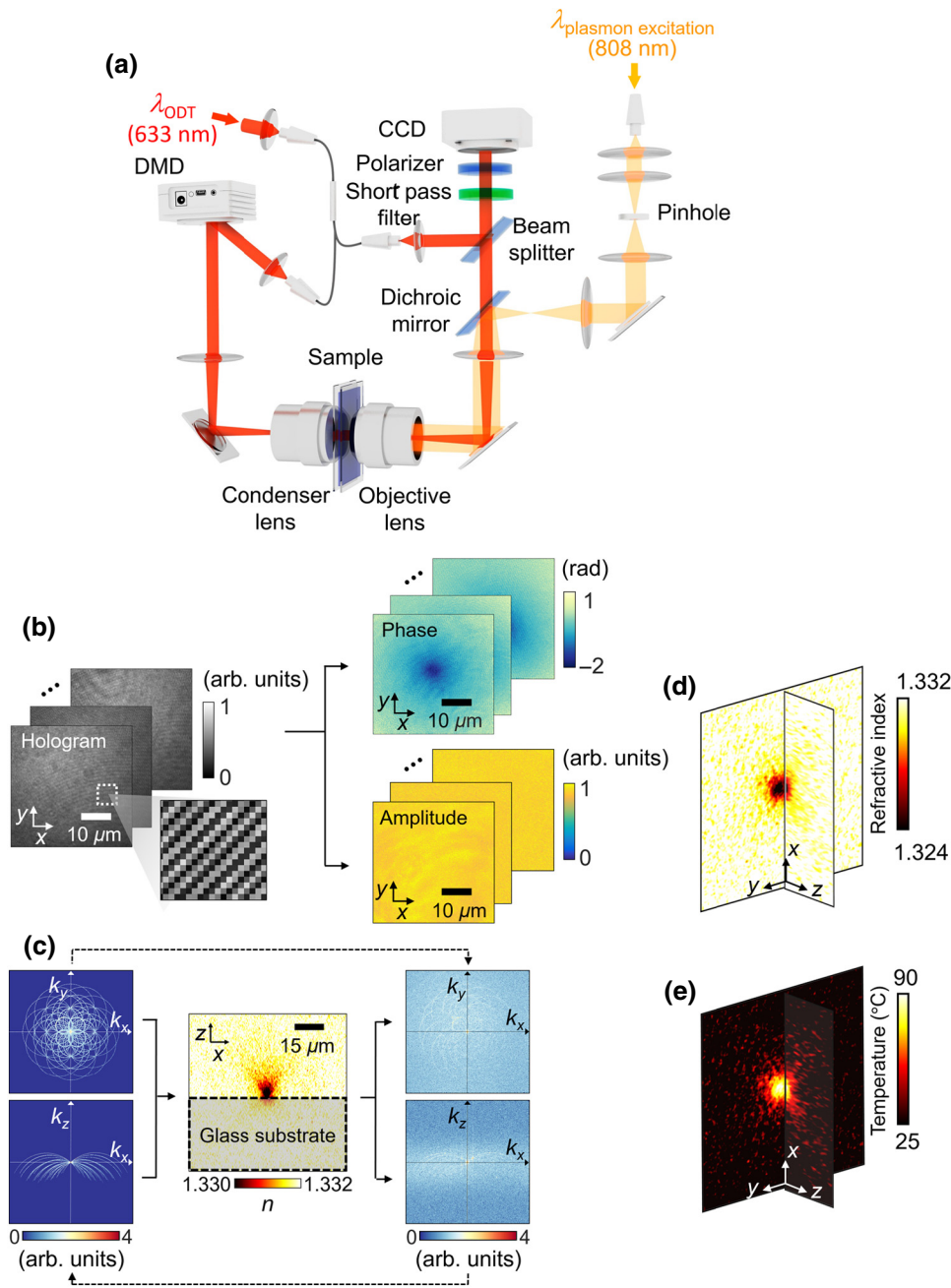


FIG. 2. (a) ODT set up for the experiment. (b) The complex optical fields, which consist of the amplitude and phase, are retrieved from multiple holograms at various illumination angles. (c) The optical fields are projected onto 3D Fourier space. Missing information originating from the limited NA of the objective lens is filled in with an iterative regularization algorithm using physical constraints. The 3D temperature distribution (e) is obtained from the measured 3D RI distribution (d) using Eq. (1).

control the incident angles of the sample beam, and 45 different illumination angles are scanned at a frame rate of 15 Hz, which implies that the total acquisition time of one RI tomogram is 3 s. The modulated sample beams are demagnified by a water immersion objective lens (NA = 1.1 LUMPLN, 60 \times , Olympus Inc., Japan) and a tube lens ($f = 250$ mm). Another high NA water immersion objective lens (NA = 1.2 UPLSAPO, 60 \times , Olympus Inc., Japan) and a second tube lens ($f = 180$ mm) are used to collect the complex optical fields diffracted from the sample. The diffracted fields interfere with the reference beam on a CMOS image

sensor (FL3-U3-13Y3M-C, FLIR Systems Inc., USA) and the image sensor records spatially modulate multiple holograms. An infrared laser diode (LD) is used as an excitation source (M9-808-015, $\lambda = 808$ nm, 150 mW, Thorlabs Inc., USA). The LD is mounted on a temperature-controlled mount (TCLDM9, Thorlabs Inc., USA) and collimated using a laser collimation lens (F230FC-780, $f = 4.51$ mm, Thorlabs Inc., USA). The LD beam is spatially filtered using a 30- μ m pinhole (P30S, Thorlabs Inc., USA) and demagnified by a set of convex lenses ($f = 250$ mm, 20 mm, and 100 mm) and a second tube lens ($f = 180$ mm).

B. Control of illumination angles using a DMD

A DMD, which consists of millions of micromirrors, is used to control the illumination angles of the sample beam by displaying a binary grating pattern, known as a Lee hologram [32,33]. The first-order diffracted beam from the binary grating is spatially filtered and used as the illumination beam. Because of the binary image on a DMD, unwanted diffracted beams are inevitable and deteriorate the quality of the measurements. To overcome this limitation, we apply a time-multiplexing illumination technique [34], which displays a sequence of discrete binary patterns to express one continuous image. In particular, to display time-averaged sinusoidal patterns in this experiment, we consecutively display four decomposed binary images for one hologram. The obtained four holograms are numerically summed by considering the temporal weights of each frame to describe an approximate sinusoidal DMD pattern. As a result, we obtain 45 holograms and confirm that the unwanted diffraction peaks in Fourier space are effectively reduced. The standard deviation of the RI distribution in the background region of the reconstructed tomograms decreases to the level of 10^{-4} . This suppression is five times larger compared to the tomogram measured with binary patterns on DMD [34,35].

C. Synthesis of gold nanorods

GNRs are synthesized by the seed-mediated method [36]. The seed solution is prepared by mixing 2.5 ml of 0.2 M cetyltrimethylammonium bromide (CTAB, Sigma), 2.5 ml of 0.5 mM HAuCl₄ (Sigma), and 300 μ l of ice-cold 0.01 M NaBH₄ (Sigma) in an ultrasonication bath at room temperature. This seed solution is aged for 2 h. The seeds are left in the growth solution at room temperature for 30 min to grow into rod-shaped structures. The growth solution consists of a mixture of 5 ml of 0.2 M CTAB, 5 ml of 1 mM HAuCl₄, 250 μ l of 4 mM AgNO₃ (Sigma), 70 μ l of 78.84 mM ascorbic acid (Sigma), and 12 μ l of seed solution. The GNRs are concentrated by centrifuge at 10 000 rpm (10200 RCF) and resuspended in ultrapure water to remove the surfactant. The GNRs are coated with thiol-terminated methoxypoly (ethylene glycol) (PEG, mPEG(5k)-SH, Nanocs) such that the GNR reaches a ratio 3 optical density (OD) and 3 mg/ml of an aqueous solution of PEG for 12 h at room temperature. Unconjugated PEG is removed using a dialysis kit (Thermo Scientific) for 2 days. The zeta potential of PEG-coated GNR is measured by a Zetasizer Nano ZS (Malvern).

Glass substrates are cleaned by successive ultrasonication in acetone, isopropyl alcohol, and deionized water, respectively, for 5 min each. Layer-by-layer coating is performed on the substrate to create a positively charged surface. Then, 10 mg/ml of poly(sodium 4-stirensulfonate) (PSS, MW \sim 15 000, Aldrich) and poly

(allylamine hydrochloride) (PAH, MW \sim 200 000, Aldrich) are prepared in 10 mM NaCl solution. The substrates are treated with three cycles of PSS and PAH solution for 5 min each, ending with PAH. Finally, 0.2 ml/cm² of 1 OD negatively charged GNR with a zeta potential -37.5 mV solution is loaded on the substrates for 12 h.

The optical property of GNR-coated glass is measured by absorbance spectroscopy (USB4000-VIS-NIR-ES, Ocean Optics). The coverage of the GNRs is calculated as 30.6%. The measurement conditions are controlled to be same as for the experiment. The central absorbance peak is detected at approximately 808 nm, which is the wavelength of the stimulation laser. The average absorbance of the samples is 0.127 OD, which implies that the extinction ratio of the sample is 25.4% for the 808-nm wavelength. For the GNRs with a 14.4-nm diameter and 50.1-nm length, the scattering is significantly lower than the absorption for the 808-nm wavelength; the portion of scattering is 10% with respect to the absorption [37,38] [Fig. 1(d)].

D. Numerical simulation

Laser-induced temperature distributions are calculated using a finite element method (FEM), for which we used commercial software (ANSYS). Construction of the simulation model for the actual experiment requires us to make two assumptions. First, the convection effect in water is ignored and only the conduction of water is considered. The beam size is less than 10 μ m, and the gap between the glass slides is as small as 40 μ m. The corresponding Rayleigh number is estimated to be 10^{-4} , which confirms that the dominant heat transfer mode is indeed heat diffusion rather than convection [39] (see Appendix C). Second, thermophysical properties of the GNR-coated glass are assumed to be the same as those of glass because the GNR occupy a much smaller volume than the glass. The boundary conditions of the analysis are implemented at an ambient temperature of 25 $^{\circ}$ C to determine the temperature distribution of water with a depth of 40 μ m. The total size of the water and glass model is $200 \times 200 \times 200 \mu\text{m}^3$. A laser with an 8.5- μ m diameter is modeled as the heat source. Since the power of the laser can be described by a Gaussian function, the Gaussian heat source is divided into ten discrete regions. The power of the discretized area is calculated and used as the input heat source.

III. RESULTS

A. Experimental demonstration

The experimental results are shown in Fig. 3. The x - y and x - z cross-section images of the reconstructed 3D RI and temperature distribution are presented in Figs. 3(a) and 3(b), respectively. The temperature sensitivity, which is the minimum distinguishable temperature change, is investigated by statistically analyzing the RI values in the

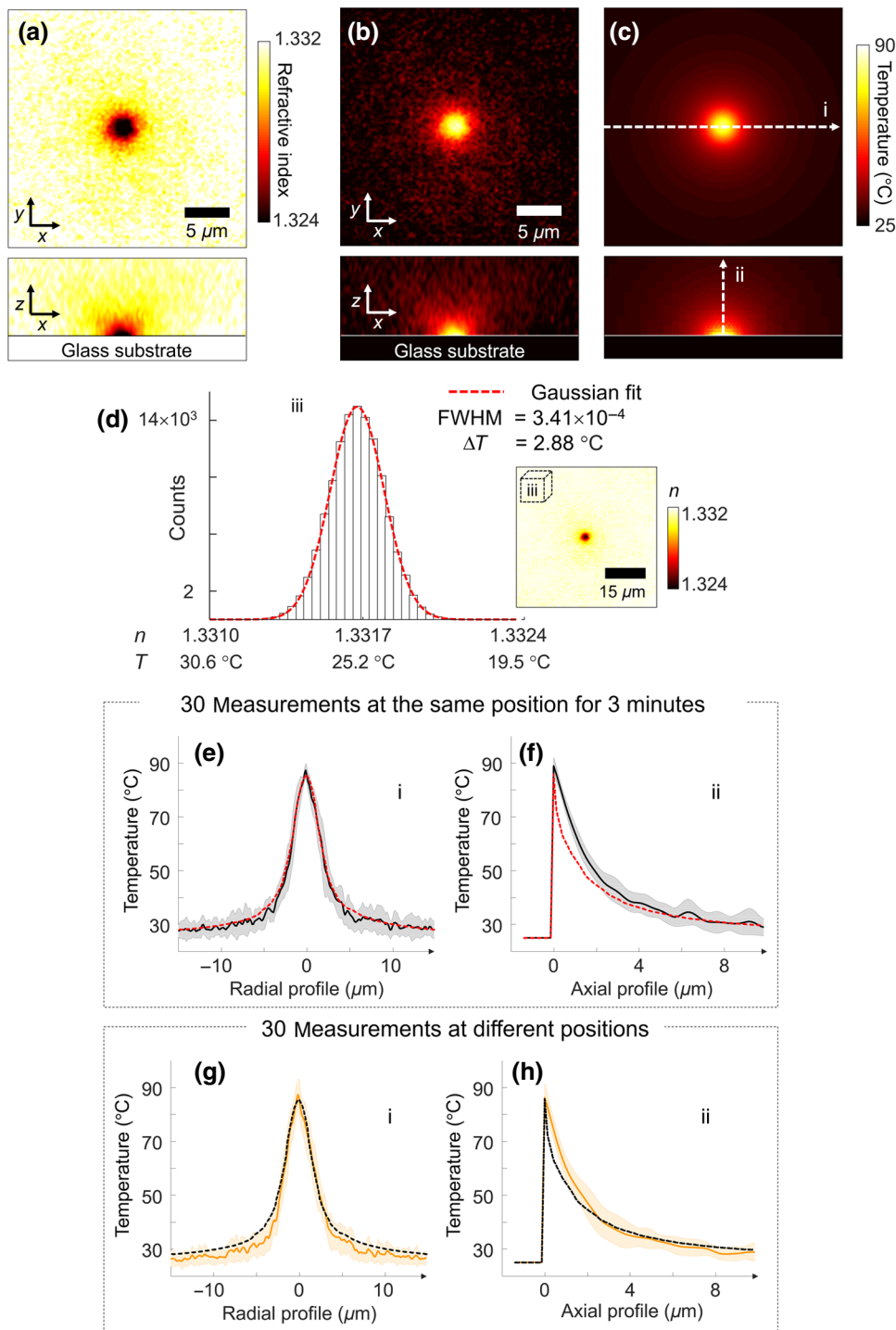


FIG. 3. Experimentally measured 3D distribution of RI and temperature. (a) x - y and x - z cross-section images of 3D RI tomogram. (b) 3D temperature distribution obtained from 3D RI distribution. (c) Result of the numerical simulation solving the steady-state heat diffusion equation, assuming the same experimental conditions. (d) Distribution of RI values in background volume. (e),(f) Temperature profiles along the radial and axial directions as white arrows (i) and (ii) as shown in Fig. 3(c). Thirty temperature distributions are measured at the same position for 3 min with the excitation laser turned on. The black line and areas represent the mean value and SD, respectively. The red dashed line is the simulation result. (g),(h) Temperature profiles extracted with the identical process used for (e) and (f). The yellow line and areas represent the mean value and SD, respectively. The black dashed line represents the calculated values.

background volume. The distribution of the reconstructed RI values is fit to the Gaussian, and the full-width half-maximum is retrieved as 3.41×10^{-4} , which indicates that the temperature sensitivity of our set up is about $2.88 \text{ }^\circ\text{C}$ [Fig. 3(d)]. The experiment is carried out under specific experimental conditions: the excitation laser is focused on the layer consisting of the GNRs. The intensity distribution of the excitation beam is presumed to be Gaussian. The Gaussian waist and total power of the excitation

beam absorbed by the GNRs are estimated as $8.5 \text{ } \mu\text{m}$ and 0.67 mW , respectively.

Two groups of measurements are acquired to demonstrate the system in dynamic equilibrium and the reproducibility of the proposed method, respectively. The first group of measurements is obtained to validate that the heated water is in the steady state. At the same measurement position with the excitation laser on, 30 temperature distributions are repeatedly measured at intervals of 3 s.

Figures 3(e) and 3(f) show the results of the measurements extracted along the radial and axial directions, indicated as white arrows (i) and (ii) in Fig. 3(c), respectively. The repetitive measurements are used to calculate the SD of the maximum temperature as 2.92 °C. This is comparable to the temperature sensitivity of the proposed method, which indicates that the system is in a steady state. The GNRs that are heated using the cw excitation source consistently supply energy to the water; thus, the temperature distribution reaches a steady state in a short time and the distributions measured over time remain constant [40].

The reproducibility of the proposed technique is verified by repeatedly measuring 30 temperature distributions at 30 different measurement locations [Figs. 3(g) and 3(h)]. The process we use to extract the radial and axial profiles is identical to that used for the first group. The SD of the maximum temperature in this experiment is observed as 4.72 °C. The fact that the SD is higher than for the minimum distinguishable temperature implies the presence of external factors. Because of the finite variance in the size and density of the GNRs, and a certain degree of anisotropy related to the GNRs' orientation, the measured temperature distributions could vary depending on positions.

The temperature profiles of both the first and second groups deviate slightly from the theoretically computed values. For the axial profiles [Figs. 3(f) and 3(h)], the deviation between the experimental and theoretical values originates from the missing information along the optical axis. That is, the lack of axial information causes the reconstructed 3D RI distributions to have an elongated shape along the axial direction [29]. Therefore, the resulting 3D temperature distributions have slowly decreasing temperature profiles along the axial direction as illustrated in Figs. 3(f) and 3(h).

A more in-depth analysis of the obtained 3D temperature distributions is carried out by measuring 30 temperature distributions for eight different excitation powers. The maximum temperatures and the distance from the origin to the isothermal positions at which the temperature increase is 25 °C along the radial and axial directions are analyzed. The determination of the maximum temperature is in good agreement with the theory, whereas both of the results of the isothermal distances deviate noticeably from the simulated results. The origin of these errors can be explained as discussed in Figs. 3(e)–3(h), considering that a greater amount of heat is transferred in the radial direction at the bottom of the water and taking into account the lack of axial information because the deviations have the same characteristics.

B. Thermodynamic analysis

We carry out a thermodynamic analysis including the 3D distribution of the heat flux density vectors and thermal

conductivity of water (Fig. 4). These thermodynamic properties are calculated from the obtained 3D temperature distributions. The heat flux vector, which is defined as the amount of heat flow in unit time and unit area, is expressed as

$$\vec{q} = -\kappa \nabla T, \quad (2)$$

where \vec{q} is the heat flux vector, κ is the thermal conductivity of the medium, and ∇T is the temperature gradient. Based on the obtained 3D temperature distribution, the heat flux vectors are visualized in 3D space to describe the way in which the heat is transferred to the surrounding medium as illustrated in Figs. 4(d)–4(g). We average 30 temperature distributions at each excitation power and assume the thermal conductivity of water is constant [41] (0.6 W/m/K at room temperature) to reduce the noise and simplify the calculations, respectively.

On the other hand, the thermal conductivity can be estimated from the measured 3D temperature distributions [Fig. 4(h)]. The integral of the heat flux vectors over an arbitrary closed surface, which contains a heat source, equals the power of the heat source delivered to the medium.

$$-\kappa \int_A \nabla T \cdot d\vec{a} = P, \quad (3)$$

where P is the power delivered to the medium and A is the arbitrary closed surface which contains the heat source. Because the integral of the temperature gradients can be calculated from the 3D temperature distribution, and the power delivered to the medium is obtained by multiplying the absorbance to the excitation laser power, one of the important thermodynamic properties, that is, the thermal conductivity of water, can be estimated from the measured 3D temperature distributions employing Eq 3. To simplify the calculation, we assume an arbitrary cylindrical surface. (see Appendix B). We calculate eight thermal conductivity values for each excitation power [Fig. 4(i)], which also shows the results of the calculations. These results show that the obtained values are comparable to the known thermal conductivity of water. The result implies that the proposed method can be applied to other transparent materials for which the thermal conductivity is unknown.

IV. DISCUSSION

In summary, we develop an optical approach that enables the 3D temperature distribution of a microscopic water layer to be determined. The proposed method makes it possible to successfully visualize the 3D temperature distributions of hot water without any labeling agents. Our approach is straightforward because the 3D temperature distribution is directly retrieved from the measured

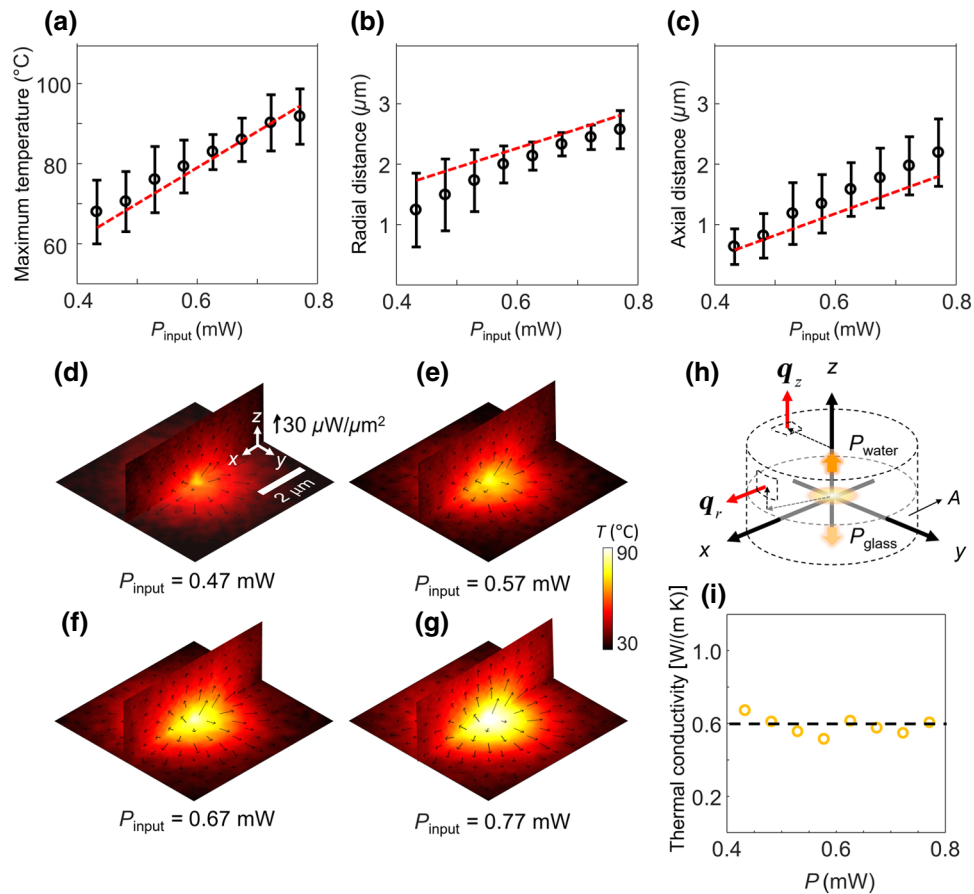


FIG. 4. Quantitative analysis of various thermodynamic properties of 3D temperature distribution. The maximum temperature (a) distances from the origin to the isothermal position at which the temperature increase is 25°C along the radial (b) and axial (c) directions are statistically analyzed. The thick black lines represent the experimental results. The red dashed lines show the result of the numerical simulation. (d–g) 3D distributions of the heat flux are obtained by taking the gradient of the 3D temperature distributions and employing the thermal conductivity of water. (h), Schematic of the calculation for the thermal conductivity of water. The total power delivered to both water and glass substrate, which is obtained by multiplying the absorbance of GNR sample, can be calculated by integrating the heat flux for an arbitrary closed surface A , which contains the heat source. The problem is simplified by specifying a cylindrical surface. (i) The result of the calculation is in good agreement with the known thermal conductivity values of water (the black dashed line, $0.6\text{ W/m}\cdot\text{K}$).

3D RI distribution. It only requires information about the temperature dependency of the RI of water. Although we demonstrate for the case of water as media, this approach is general and can be applied to other optically transparent media such as oil [42].

The measured 3D temperature distributions describe the comprehensive thermodynamic situation without considering any external variables. We suggest that the proposed method can be applied to identify thermodynamic properties, such as the 3D distribution of the heat flux vectors and the thermal conductivity of an unknown fluidic system. On the other hand, improved temperature sensitivity can be achieved by employing a system with less noise, a common-path interferometric scheme [35]. The present method can also be readily applied to various studies, including temperature measurements around a single nanoparticle. It could be potentially further extended to

investigate the temperature distribution around a single gold nanoparticle injected into the membranes for cancer therapy [43]. The dynamic behavior of a system can also be addressed using the present method; transient temperature evolution can be measured by employing a faster acquisition and reconstruction configuration in the future [44]. We envision that our method will facilitate an understanding of the various thermal phenomena in a microscopic fluidic system and foresee its use in various biomedical applications in the future.

ACKNOWLEDGMENTS

S.S. and Y.K.P. have financial interests in Tomocube Inc., a company that commercializes ODT instruments and is one of the sponsors of the work.

This work was supported by KAIST, BK21+ program, Tomocube, and National Research Foundation of Korea (Grants No. 2015R1A3A2066550, No. 2017M3C1A3013 923, No. 2018K000396, No. 2014K1A3A1A09063027, No. 2015R1A2A1A10055060, and No. 2015R1A2A1A09 003605). This research was also partly supported by KAIST Institute for the NanoCentury.

APPENDIX A: TEMPERATURE DEPENDENCY OF RI CHANGE OF WATER AND GLASS SUBSTRATE

We refer to Schiebener *et al.* [17] and Toyoda and Yabe [30]. RI of water from 20 °C to 90 °C at 0.1 MPa (1 atm) and 632.8 nm is used (Table 7 of Schiebener *et al.* [17]). The third-order polynomial fit curve (Fig. 5) is estimated from the obtained RI values of water at each temperature and is used to convert the 3D RI distribution into a 3D temperature distribution.

At the interface between the glass substrate and water, the temperature profiles along the axial direction are assumed to be continuous [40] so that we can compare the maximum RI change of both water and glass substrate at the same temperature increase. When the temperature of water increases from 25 °C to 100 °C, the RI change is approximately $|\Delta n_{\text{water}}| \sim 1.5 \times 10^{-2}$, while the RI change of fused silica is estimated to be $|\Delta n_{\text{glass}}| \sim 9.3 \times 10^{-4}$. As a consequence, we notice that the maximum RI change of glass substrate is less than 6% that of the RI change of water, which supports the assumption we use in the experiment: the RI change of the glass substrate is negligible.

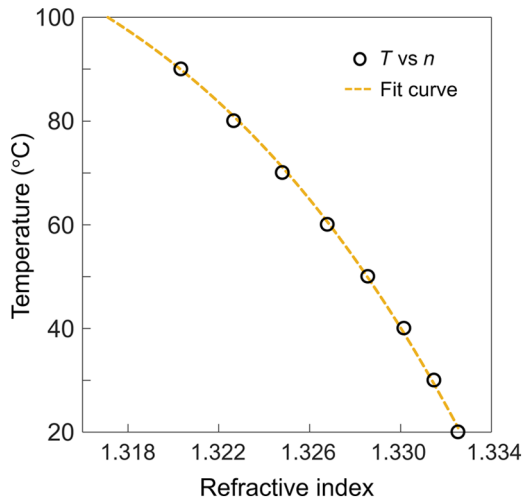


FIG. 5. Quantitative analysis of various thermodynamic properties of 3D temperature distribution. Thirty temperature distributions are measured for each of eight different values of the excitation power

APPENDIX B: CALCULATION OF THERMAL CONDUCTIVITY

Heat flux vector describes heat transfer in a medium and is defined as the gradient of temperature distributions. A divergence of heat flux, on the other hand, indicates a power density of a heat source. Because of the GNRs, a two-dimensional heat source is deposited at the interface of the water and glass substrate, the heat generated from the source must be transferred to both sides, and we notice that the ratio of the total heat delivered to each material is determined by the ratio of the thermal conductivity of each medium [45,46].

$$P_{\text{water}} : P_{\text{glass}} = \kappa_{\text{water}} : \kappa_{\text{glass}}, \quad (\text{B1})$$

where P_{water} is the power transferred to the water, P_{glass} is the power delivered to the glass substrate, κ_{glass} is the thermal conductivity of glass, and κ_{water} is the thermal conductivity of water that we are trying to calculate. Assuming that we do not have *a priori* information of the thermal conductivity of water, we define an experimental parameter P_{exp} by omitting the unknown thermal conductivity in Eq. (3).

$$P_{\text{exp}} = - \int_A \nabla T \cdot d\vec{a}, \quad (\text{B2})$$

where A is now the surface region over the water excluding the area of the glass substrate. From the known absorption efficiency of the heat source, we determine an initial input power P_{input} , which is absorbed and emitted by GNRs and substitute P_{glass} for P_{water} in Eq. (B1). Combining Eqs. (B1) and (B2), we can estimate the thermal conductivity of water,

$$\kappa_{\text{water}} = \frac{P_{\text{input}}}{P_{\text{exp}}} \kappa_{\text{glass}}. \quad (\text{B3})$$

We use 1.4 W/m/K for the thermal conductivity of the glass substrate. To simplify the calculation, we integrate heat flux vectors for an arbitrary cylindrical surface over the region of water.

APPENDIX C: CONTRIBUTION OF HEAT CONDUCTION AND CONVECTION

Rayleigh number (Ra) of the fluidic system implies the contribution of the convection to the heat transfer. Ra is defined as

$$\text{Ra} = \frac{VL}{\alpha}, \quad (\text{C1})$$

where V is the velocity of the flow, L is the size of the heat source, and α is the diffusivity of the water [39]. In the practical experiment, $V = 10^{-6}$ m/s, $L = 8.5 \mu\text{m}$, and $\alpha = 1.4 \times 10^{-7}$ m²/s. The calculated Ra in the experiment is the order of 10^{-4} and it implies that the

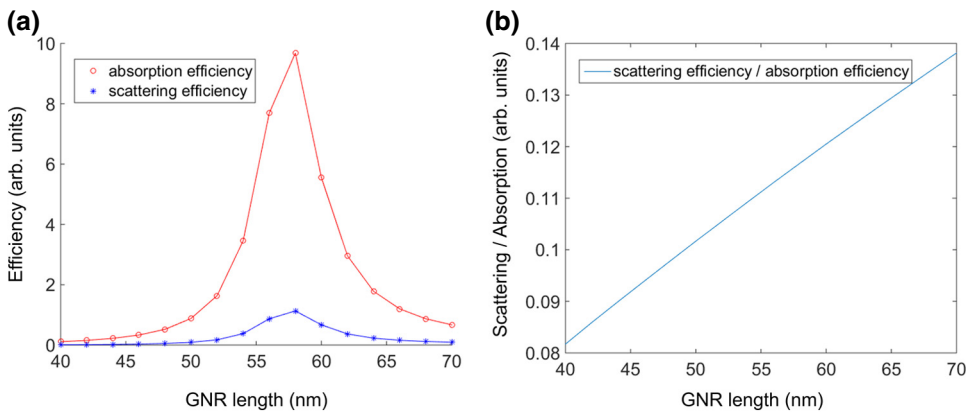


FIG. 6. Quantitative analysis of various thermodynamic properties of 3D temperature distribution. Thirty temperature distributions are measured for each of eight different values of the excitation power.

contribution of the convection to the temperature distribution is negligible [43].

APPENDIX D: THE TIMESCALE TO THE STEADY-STATE

In the experiment, the 3D temperature distribution of water reaches the steady-state in quite a short time according to the relation

$$\tau = \frac{L^2}{\alpha}, \quad (\text{D1})$$

where L is the dimension of the heat source and α is the diffusivity of the water [39]. The intensity distribution of the heat source is a 2D Gaussian of $8.5\text{-}\mu\text{m}$ waists, and the diffusivity of water is $1.4 \times 10^{-7} \text{ m}^2/\text{s}$, which implies that τ is the order of 10^{-4} and the system reaches the steady-state in the time scale of microseconds. After heating, the temperature distribution remains constant because the continuous wave LD is employed in the practical experiment.

APPENDIX E: THE PORTION OF ABSORPTION AND SCATTERING OF GNRS

We simulate the boundary element method to solve the scattering and absorption problem of GNRS of 14.4-nm diameter and 50.1-nm length for an 808-nm wave. The result indicates that the scattering efficiency of GNR is 10% of its absorption efficiency [37,38]; thus, we can neglect the effect of scattering (Fig. 6).

- [1] P. K. Jain, I. H. El-Sayed, and M. A. El-Sayed, Au nanoparticles target cancer, *Nano Today* **2**, 18 (2007).
- [2] S. Yoo, S. Hong, Y. Choi, J.-H. Park, and Y. Nam, Photothermal inhibition of neural activity with near-infrared-sensitive nanotransducers, *ACS Nano* **8**, 8040 (2014).
- [3] S. Yoo, R. Kim, J.-H. Park, and Y. Nam, Electro-optical neural platform integrated with nanoplasmonic inhibition interface, *ACS Nano* **10**, 4274 (2016).

- [4] P. Ghosh, G. Han, M. De, C. K. Kim, and V. M. Rotello, Gold nanoparticles in delivery applications, *Adv. Drug Deliv. Rev.* **60**, 1307 (2008).
- [5] X. Miao, B. K. Wilson, and L. Y. Lin, Localized surface plasmon assisted microfluidic mixing, *Appl. Phys. Lett.* **92**, 124108 (2008).
- [6] S. Sade, L. Nagli, and A. Katzir, Scanning near field infrared radiometry for thermal imaging of infrared emitters with subwavelength resolution, *Appl. Phys. Lett.* **87**, 101109 (2005).
- [7] M. De Angelis, P. Matteini, F. Ratto, R. Pini, S. Coppola, S. Grilli, V. Vespini, and P. Ferraro, Plasmon resonance of gold nanorods for all-optical drawing of liquid droplets, *Appl. Phys. Lett.* **103**, 163112 (2013).
- [8] L. Battista, L. Mecozzi, S. Coppola, V. Vespini, S. Grilli, and P. Ferraro, Graphene and carbon black nano-composite polymer absorbers for a pyro-electric solar energy harvesting device based on LiNbO_3 crystals, *Appl. Energy* **136**, 357 (2014).
- [9] J. S. Donner, S. A. Thompson, M. P. Kreuzer, G. Baffou, and R. Quidant, Mapping intracellular temperature using green fluorescent protein, *Nano Lett.* **12**, 2107 (2012).
- [10] S. Arai, M. Suzuki, S.-J. Park, J. S. Yoo, L. Wang, N.-Y. Kang, H.-H. Ha, and Y.-T. Chang, Mitochondria-targeted fluorescent thermometer monitors intracellular temperature gradient, *Chem. Commun.* **51**, 8044 (2015).
- [11] G. Baffou, M. Kreuzer, F. Kulzer, and R. Quidant, Temperature mapping near plasmonic nanostructures using fluorescence polarization anisotropy, *Opt. Express* **17**, 3291 (2009).
- [12] F. Vetrone, R. Naccache, A. Zamarrón, A. J. de la Fuente, F. Sanz-Rodríguez, L. M. Maestro, E. M. Rodríguez, D. Jaque, J. G. Solé, and J. A. Capobianco, Temperature sensing using fluorescent nanothermometers, *ACS Nano* **4**, 3254 (2010).
- [13] G. Baffou, P. Bon, J. Savatier, J. Polleux, M. Zhu, M. Merlin, H. Rigneault, and S. Monneret, Thermal imaging of nanostructures by quantitative optical phase analysis, *ACS Nano* **6**, 2452 (2012).
- [14] P. Bon, N. Belaid, D. Lagrange, C. Bergaud, H. Rigneault, S. Monneret, and G. Baffou, Three-dimensional temperature imaging around a gold microwire, *Appl. Phys. Lett.* **102**, 244103 (2013).

- [15] S. De Nicola, A. Finizio, P. Ferraro, and G. Pierattini, An interferometric technique based on Fourier fringe analysis for measuring the thermo-optic coefficients of transparent materials, *Opt. Commun.* **159**, 203 (1999).
- [16] M. De Angelis, S. De Nicola, P. Ferraro, A. Finizio, and G. Pierattini, Liquid refractometer based on interferometric fringe projection, *Opt. Commun.* **175**, 315 (2000).
- [17] P. Schiebener, J. Straub, J. Levelt Sengers, and J. Gallagher, Refractive index of water and steam as function of wavelength, temperature and density, *J. Phys. Chem. Ref. Data* **19**, 677 (1990).
- [18] E. Wolf, Three-dimensional structure determination of semi-transparent objects from holographic data, *Opt. Commun.* **1**, 153 (1969).
- [19] K. Kim, J. Yoon, S. Shin, S. Lee, S.-A. Yang, and Y. Park, Optical diffraction tomography techniques for the study of cell pathophysiology, *J. Biomed. Photonics Eng.* **2**, 020201 (2016).
- [20] Y. Park, C. Depeursinge, and G. J. N. P. Popescu, Quantitative phase imaging in biomedicine, *Nat. Photonics* **12**, 578 (2018).
- [21] V. Amendola, R. Pilot, M. Frascioni, O. M. Maragò, and M. A. Iati, Surface plasmon resonance in gold nanoparticles: a review, *J. Phys.: Condens. Matter* **29**, 203002 (2017).
- [22] S. W. Prescott and P. Mulvaney, Gold nanorod extinction spectra, *J. Appl. Phys.* **99**, 123504 (2006).
- [23] M. A. El-Sayed, Some interesting properties of metals confined in time and nanometer space of different shapes, *Acc. Chem. Res.* **34**, 257 (2001).
- [24] T. Kim, R. Zhou, L. L. Goddard, and G. Popescu, Solving inverse scattering problems in biological samples by quantitative phase imaging, *Laser Photonics Rev.* **10**, 13 (2016).
- [25] D. Jin, R. Zhou, Z. Yaqoob, and P. T. C. So, Tomographic phase microscopy: principles and applications in bioimaging [Invited], *J. Opt. Soc. Am. B* **34**, B64 (2017).
- [26] S. Shin, K. Kim, J. Yoon, and Y. Park, Active illumination using a digital micromirror device for quantitative phase imaging, *Opt. Lett.* **40**, 5407 (2015).
- [27] E. Cuche, P. Marquet, and C. Depeursinge, Spatial filtering for zero-order and twin-image elimination in digital off-axis holography, *Appl. Opt.* **39**, 4070 (2000).
- [28] A. C. Kak and M. Slaney, *Principles of Computerized Tomographic Imaging* (Society for Industrial and Applied Mathematics, Philadelphia, 2001), Classics in applied mathematics, 33.
- [29] J. Lim, K. Lee, K. H. Jin, S. Shin, S. Lee, Y. Park, and J. C. Ye, Comparative study of iterative reconstruction algorithms for missing cone problems in optical diffraction tomography, *Opt. Express* **23**, 16933 (2015).
- [30] T. Toyoda and M. Yabe, The temperature dependence of the refractive indices of fused silica and crystal quartz, *J. Phys. D: Appl. Phys.* **16**, L97 (1983).
- [31] Y. Sung and R. R. Dasari, Deterministic regularization of three-dimensional optical diffraction tomography, *JOSA A* **28**, 1554 (2011).
- [32] W.-H. Lee, Binary computer-generated holograms, *Appl. Opt.* **18**, 3661 (1979).
- [33] S. Shin, K. Kim, T. Kim, J. Yoon, K. Hong, J. Park, and Y. Park, in Proc. of SPIE (2016), pp. 971814.
- [34] K. Lee, K. Kim, G. Kim, S. Shin, and Y. J. O. L. Park, Time-multiplexed structured illumination using a DMD for optical diffraction tomography, *Opt. Lett.* **42**, 999 (2017).
- [35] S. Shin, Y. Kim, K. Lee, K. Kim, Y.-J. Kim, H. Park, and Y. Park, Common-path diffraction optical tomography with a low-coherence illumination for reducing speckle noise (2015).
- [36] B. Nikoobakht and M. A. El-Sayed, Preparation and growth mechanism of gold nanorods (NRs) using seed-mediated growth method, *Chem. Mater.* **15**, 1957 (2003).
- [37] G. S. He, J. Zhu, K.-T. Yong, A. Baev, H.-X. Cai, R. Hu, Y. Cui, X.-H. Zhang, and P. Prasad, Scattering and absorption cross-section spectral measurements of gold nanorods in water, *J. Phys. Chem. C* **114**, 2853 (2010).
- [38] P. K. Jain, K. S. Lee, I. H. El-Sayed, and M. A. El-Sayed, Calculated absorption and scattering properties of gold nanoparticles of different size, shape, and composition: Applications in biological imaging and biomedicine, *J. Phys. Chem. B* **110**, 7238 (2006).
- [39] J. S. Donner, G. Baffou, D. McCloskey, and R. Quidant, Plasmon-assisted optofluidics, *ACS Nano* **5**, 5457 (2011).
- [40] G. Baffou and H. Rigneault, Femtosecond-pulsed optical heating of gold nanoparticles, *Phys. Rev. B* **84**, 035415 (2011).
- [41] M. L. Ramires, C. A. Nieto de Castro, Y. Nagasaka, A. Nagashima, M. J. Assael, and W. A. Wakeham, Standard reference data for the thermal conductivity of water, *J. Phys. Chem. Ref. Data* **24**, 1377 (1995).
- [42] K. Kim, J. Yoon, and Y. J. O. L. Park, Large-scale optical diffraction tomography for inspection of optical plastic lenses, *Opt. Lett.* **41**, 934 (2016).
- [43] A. S. Urban, T. Pfeiffer, M. Fedoruk, A. A. Lutich, and J. Feldmann, Single-step injection of gold nanoparticles through phospholipid membranes, *ACS Nano* **5**, 3585 (2011).
- [44] K. Kim, K. S. Kim, H. Park, J. C. Ye, and Y. Park, Real-time visualization of 3-D dynamic microscopic objects using optical diffraction tomography, *Opt. Express* **21**, 32269 (2013).
- [45] S. J. Blundell and K. M. Blundell, *Concepts in Thermal Physics* (OUP, Oxford, 2009).
- [46] S. O. Kasap, *Principles of Electronic Materials and Devices* (McGraw-Hill, New York, 2006), Vol. 2.